



# CHORUS

This is the accepted manuscript made available via CHORUS. The article has been published as:

## Binding a hopfion in a chiral magnet nanodisk

Yizhou Liu, Roger K. Lake, and Jiadong Zang

Phys. Rev. B **98**, 174437 — Published 28 November 2018

DOI: [10.1103/PhysRevB.98.174437](https://doi.org/10.1103/PhysRevB.98.174437)

# Binding a Hopfion in Chiral Magnet Nanodisk

Yizhou Liu,<sup>1,\*</sup> Roger K. Lake,<sup>1,†</sup> and Jiadong Zang<sup>2,‡</sup>

<sup>1</sup>*Department of Electrical and Computer Engineering,  
University of California, Riverside, California 92521, USA*

<sup>2</sup>*Department of Physics and Materials Science Program,  
University of New Hampshire, Durham, New Hampshire 03824, USA*

Hopfions are three-dimensional (3D) topological textures characterized by the integer Hopf invariant  $Q_H$ . Here, we present the realization of a zero-field, stable hopfion spin texture in a magnetic system consisting of a chiral magnet nanodisk sandwiched by two films with perpendicular magnetic anisotropy. The preimages of the spin texture and numerical calculations of  $Q_H$  show that the hopfion has  $Q_H = 1$ . Furthermore, another non-trivial state that includes a monopole-antimonopole pair (MAP) is also stabilized in this system. By applying an external magnetic field, hopfion and MAP states with the same polarization can be switched between each other. The topological transition between the hopfion and the MAP state involves a creation (annihilation) of the MAP and twist of the preimages. Our work paves the way to study non-trivial 3D topological spin textures and stimulates more investigations in the field of 3D spintronics.

## I. INTRODUCTION

A topological soliton carries an integer topological index that cannot be changed by a continuous deformation [1]. A celebrated example is the skyrmion, a two-dimensional (2D) topological soliton originated from the Skyrme model [2], which can be characterized by the skyrmion number (or winding number) [3]. The addition of a third spatial dimension brings more diverse and complicated topological solitons, such as rings, links and knots [4–6]. Some of these three-dimensional (3D) topological solitons are “hopfions”, since they can be classified by the Hopf invariant ( $Q_H$ ) [7], a topological index of the homotopy group  $\Pi_3(S^2)$  that can be interpreted as the linking number [8]. Due to their complex structures and models, the detailed study of the hopfion was properly established not long ago in terms of toroidal coordinates [9, 10]. Hopfions have been observed in a variety of physical systems including fluids, optics, liquid crystals, Bose-Einstein condensates, etc. [11–17] But their observation in magnetic materials remains elusive.

In magnetic systems, topological solitons in one dimension and two dimensions such as domain walls and vortices have been extensively studied over the past few decades. Much of the recent attention is attracted by the magnetic skyrmions residing in magnetic materials with the antisymmetric Dzyaloshinskii-Moriya interaction (DMI) [18–20]. Skyrmions are proposed to be promising candidate for spintronic applications due to their prominent features such as the nanoscale size and low driving current density [21, 22]. Although numerous studies have been made on the low-dimensional topolog-

ical solitons, 3D topological solitons like hopfions have still not been well explored in nanomagnetism. Understanding the static and dynamical properties of these 3D topological solitons are not only of fundamental interest, but may also enable potential applications.

In ferromagnetic systems, only a few theoretical proposals predict the existence of hopfions, but only in the dynamical regime [23–25]. In chiral ferromagnetic liquid crystals, such 3D topological solitons can be stabilized via complicated high order interactions and specific boundary conditions [15, 16, 26]. However, these interactions and boundary conditions are difficult to achieve and their counterparts are not obvious in magnets. It has been recently proposed that a higher order exchange interaction and an external magnetic field will stabilize a metastable hopfion in a frustrated magnet [27], but how to create such metastable state is not clear.

Here, we show that a  $Q_H = 1$  hopfion can be enabled in a chiral magnet nanodisk in the absence of external magnetic fields. The nanodisk is sandwiched by two magnetic layers with perpendicular magnetic anisotropy (PMA) to nucleate the hopfion in between. The hopfion is identified by both the preimages and the numerical calculations of  $Q_H$ . Associated with the hopfion, another non-trivial state that includes a monopole-antimonopole pair (MAP) is also stabilized at zero fields in this structure. This MAP state is similar to the so-called toron structure in chiral liquid crystals [28]. Furthermore, the hopfion can be switched into a MAP state with the same polarization by an applied magnetic field, and vice versa. The topological transition between the hopfion state and the MAP state involves the creation (annihilation) of the monopole-antimonopole pair and a twist of the preimages.

## II. STABLE HOPFION AND MAP STATE

We consider a chiral magnet nanodisk sandwiched by two PMA magnetic thin layers with 10 nm thickness,

\* yliu062@ucr.edu

Present Address: Beijing National Laboratory for Condensed Matter Physics, Institute of Physics, Chinese Academy of Sciences, Beijing 100190, China

† rlake@ece.ucr.edu

‡ Jiadong.Zang@unh.edu

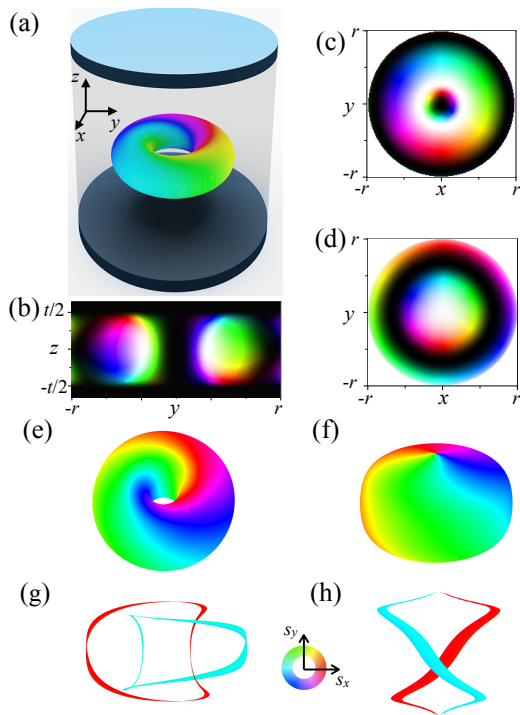


FIG. 1. (a) Schematic of the proposed structure. The thin disks at the top and bottom are the magnetic films with PMA. The transparent region in the middle is the chiral magnet nanodisk. The coordinate system is shown as inset. The color ring at the center represents the set of preimages with  $s_z = 0$  of a  $Q_H = 1$  hopfion. The hopfion cross-section in the  $y - z$  plane is shown in (b). (c), (d) The cross-sectional spin textures in the  $x - y$  plane ( $z=0$ ) for the hopfion (c) and MAP (d) in a chiral magnet nanodisk with radius  $r = 100$  nm ( $1.43L_D$ ) and thickness  $t = 70$  nm ( $1L_D$ ). (e), (f) The set of preimages with  $s_z = 0$  for the hopfion and MAP, respectively. (g), (h) The preimages of  $\mathbf{s} = (-1, 0, 0)$  (cyan) and  $\mathbf{s} = (1, 0, 0)$  (red) for the hopfion (e) and MAP (f). In the color scheme, black indicates  $s_z = -1$  and white indicates  $s_z = 1$ . The color wheel is for  $s_z = 0$ .

as shown in Fig. 1(a). An isotropic bulk type DMI is employed to model the chiral magnet. The Hamiltonian of this system is given by

$$\mathcal{H} = \int dr^3 [-A(\nabla\mathbf{s})^2 - (1-p)D\mathbf{s} \cdot (\nabla \times \mathbf{s}) - pK_u(s_z)^2 + E_d], \quad (1)$$

where  $A$  and  $D$  are the exchange and DMI constant, respectively,  $K_u$  is the PMA constant, and  $p$  is 0 in the chiral magnet nanodisk and 1 in two PMA layers.  $E_d$  is the magnetic dipole-dipole interaction (DDI). It depends on the exact shape of the system. The DDI can stabilize spin textures such as zero-field target skyrmion in confined geometries [29–32]. The effect of DDI here is discussed in details in Appendix.

We minimize the Hamiltonian (1) in the nanodisk structure with different initial states (for details of the simulation methods and parameters, see Appendix). Af-

ter minimizing the energy, we find two stable non-trivial states at zero-field, the the MAP state and the  $Q_H = 1$  hopfion state. The  $s_x$  and  $s_y$  components of the spin textures of both states are plotted in Fig. 1, where normalized lengths are provided in terms of the helical period of the chiral magnet,  $L_D = 4\pi A/D$ . The hopfion spin texture consists of a  $2\pi$  twisted skyrmion tube with its two ends glued together as shown in Fig. 1(a,b). A cross-section in the  $y - z$  plane consists of a skyrmion-antiskyrmion pair, as shown in Fig. 1(b). A cross-section in the  $x - y$  plane, shown in Fig. 1(c), has a  $2\pi$  vortex in which spin rotates by  $2\pi$  going from the center to the periphery [34]. On the other hand, the cross-section of the MAP state in the  $x - y$  plane consists of a skyrmion at the center and an edge state at the boundary, as shown in Fig. 1(d). It is similar to a typical target skyrmion state recently observed in FeGe nanodisk [32].

To further visualize and understand the spin configurations of the hopfion and MAP in 3D, we plot their preimages using Spirit [35]. A preimage is the region in 3D real space that contains spins with the same orientations. It is a Hopf map of a point on the  $S^2$  unit sphere to 3D space. We first plot the set of preimages of all spins with  $s_z = 0$  for the hopfion (Fig 1(e)) and MAP (Fig. 1(f)), which corresponds to a Hopf map from the equator of the  $S^2$  unit sphere to the 3D space. Two preimages are topologically distinct as characterized by different genus  $g$ , i.e., the number of holes. The preimage of the hopfion forms a torus with  $g = 1$ , whereas the preimage of the MAP is a trivial surface with  $g = 0$ , which satisfies the Poincaré-Hopf theorem [36].

The Hopf invariant, also called the linking number, counts the number of links between two arbitrary closed-loop preimages. Therefore, preimages of two arbitrary spins must form closed loops that are linked with each other. These features can be identified by the preimages of  $\mathbf{s} = (1, 0, 0)$  and  $\mathbf{s} = (-1, 0, 0)$  for the hopfion (Fig. 1(g)) and MAP (Fig. 1(h)). For the hopfion, two closed-loop preimages are formed and linked with each other once.  $Q_H = 1$  in this case, and the topology of the hopfion state in this system is confirmed. In contrast, the MAP does not have closed-loop preimages and thus no links. Monopole and antimonopole are source and drain of all preimages. The two MAP preimages of  $\mathbf{s} = (1, 0, 0)$  and  $\mathbf{s} = (-1, 0, 0)$  join at the monopole and antimonopole indicating their singular natures. The MAP is considered a defect state, while the hopfion is a smooth spin texture with no singularity. These preimages successfully reflect the topological natures of the two states.

### III. HOPF INVARIANT CALCULATION

Other than the linking number of preimages, topology of the hopfion can also be confirmed by directly calculating the Hopf invariant. The integral form of the Hopf

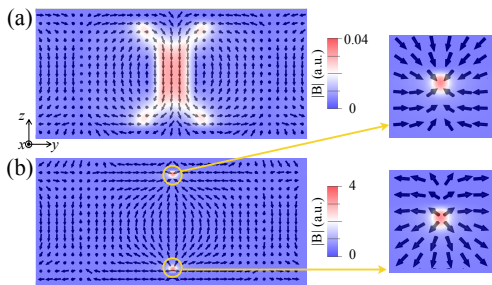


FIG. 2. (a), (b) The emergent magnetic field  $\mathbf{B}$  in the  $y$ - $z$  plane ( $x=0$ ) for hopfion (a) and MAP (b) using the same geometry as Fig. 1. Insets show the enlarged  $\mathbf{B}$  plot at the monopole and antimonopole, which has opposite monopole charges.

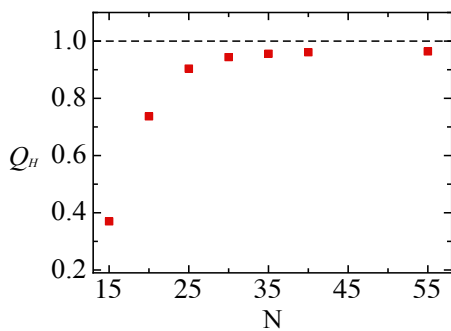


FIG. 3. Numerical calculations of the Hopf invariant  $Q_H$  for different meshes. The total number of grid points  $N_{tot} = N^3$ .

invariant in real space can be expressed as [37, 38]

$$Q_H = - \int \mathbf{B} \cdot \mathbf{A} d\mathbf{r}, \quad (2)$$

where  $B_i = \frac{1}{8\pi} \epsilon_{ijk} \mathbf{s} \cdot (\nabla_j \mathbf{s} \times \nabla_k \mathbf{s})$  is the emergent magnetic field associated with the spin textures, and  $\mathbf{A}$  is any vector potential that satisfies the magnetostatic equation  $\nabla \times \mathbf{A} = \mathbf{B}$ . The Hopf number is invariant under a gauge transformation  $\mathbf{A} \rightarrow \mathbf{A} + \nabla\chi$  only when the emergent field  $\mathbf{B}$  is free of singularities, *i.e.*,  $\nabla \cdot \mathbf{B} = 0$ . Cross-sections in the  $y$ - $z$  plane of the emergent magnetic fields  $\mathbf{B}$  of the hopfion and MAP states are shown in Fig. 2. The emergent  $\mathbf{B}$  field of the hopfion shown in Fig. 2(a) flows smoothly and streams intensively near the center of the nanodisk. In contrast, the emergent  $\mathbf{B}$  field of the MAP shown in Fig. 2(b) clearly presents two magnetic monopoles with opposite charges near the top and bottom surface. The Hopf invariant is thus ill-defined for the MAP state, and it is well defined for the hopfion texture.

The vector potential  $\mathbf{A}$  is solved in momentum space with the Coulomb gauge  $\mathbf{k} \cdot \mathbf{A} = 0$ , and then  $Q_H$  is also computed in momentum space [39]. To carry out the numerical integral, discrete grids in the momentum space

are employed. As shown in Fig. 3, as the grid number ( $N_{tot}$ ) increases,  $Q_H$  rapidly converges to 1. We thus obtain a Hopf invariant of  $Q_H = 0.96$  for the hopfion spin texture under investigation. Here  $Q_H$  is slightly deviated from an integer due to the finite size and open boundary condition. The manifold is not compact, as indicated by the edge state around the disk boundary. Nevertheless, the Hopf invariant is close to 1, and the topological nature of the hopfion is further confirmed.

#### IV. TOPOLOGICAL TRANSITION BETWEEN HOPFION AND MAP STATE

At zero external magnetic field, two states with opposite spins share the same energy. Therefore, stable hopfion and MAP states each have two polarizations, *i.e.* spin points up or down at their cores. As shown in Fig. 4, the MAP state has lower energy than the hopfion state at zero magnetic field. But they can be switched between each other by sweeping an external magnetic field. When applying a magnetic field in the same (opposite) direction with the MAP (hopfion) polarization, the MAP (hopfion) can be switched into a hopfion (MAP) with the same polarization. Thus, despite the MAP state having lower energy, the hopfion state can still be realized by using an applied field. **Here, we mainly focus on the switching between the hopfion and MAP with the same polarization, but it is also possible to switch between MAP states with opposite polarizations using a large field to saturating spins in the opposite direction as indicated by the bottom inset of Fig. 4.**

Since the hopfion is topologically protected by the nonzero Hopf invariant, a topological transition must take place in the switching between the hopfion and MAP states. To investigate this topological transition, we performed a minimal energy path (MEP) calculation between these two states in the same geometry with Fig. 1 [40–42]. The MEP calculation is carried out using the geodesic nudged elastic band method associated with the Hamiltonian in Eq. (1). The stable spin textures from the energy minimizations are employed as the initial states in the MEP calculation.

Results from the MEP calculation are shown in Fig. 5(a). There exists an energy barrier between the hopfion and the MAP state. Thus, an activation energy is required to enable the transition from the hopfion (MAP) to MAP (hopfion) state. To capture details of the topological transition, we plot preimages of  $\mathbf{s} = (1,0,0)$  and  $\mathbf{s} = (-1,0,0)$  at the initial hopfion state, the barrier peak, the intermediate MEP state and the final MEP state (Fig. 5(b)-(e)). Transitioning from the hopfion state in (b) to the intermediate state (d), the two linked preimages break and reconnect generating the monopole-antimonopole pair with a  $2\pi$  rotation. The two preimages are then topologically equivalent to those of the MAP state in Fig. 5(e), although they are twisted by  $2\pi$ . Re-

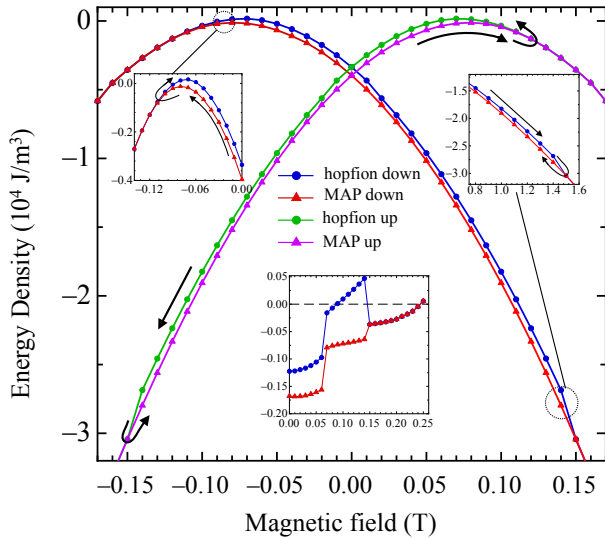


FIG. 4. Energy density plot of the hopfion and MAP state as a function of external magnetic field. Black arrows indicate the field sweeping directions and the switching events. **Top insets show the enlarged details near the switching point. Bottom inset plots the relative energy density of the hopfion and MAP state to the trivial state (ferromagnetic state at high field or conical like state at low field) with positive polarization. Below 0.25 T, MAP is the ground state and hopfion also has lower energy than the trivial state below 0.09 T. The ferromagnetic state becomes the ground state only when the field is above 0.25 T.** The nanodisk geometry is the same as in Fig. 1.

laxing from point (d) to to the MAP state of point (e), the preimages untwist to  $\pi$ , while the monopole and antimonopole move towards the top and bottom surface, respectively. Videos of the transition also capture the transformation from a torus ( $g = 1$ ) to a trivial surface ( $g = 0$ ) for the preimages of  $s_z = 0$  (see movies in the Supplemental Materials). To create a hopfion from a MAP state, the reverse process is applied. The preimages first rotate from  $\pi$  to  $2\pi$ . The monopole–antimonopole pair move towards each other until they eliminate each other. Then each preimage becomes close-looped and linked with the other preimage.

## V. PHASE DIAGRAM OF HOPFION AND MAP

Since the hopfion is a 3D spin texture, a finite radius and thickness of the chiral magnet nanodisk are required to stabilize it, and the length scale is determined by the helical period  $L_D$  of the chiral magnet. This is confirmed by the calculated phase diagram of a stable hopfion as a function of the nanodisk radius  $r$  and thickness  $t$  shown in Fig. 6. When  $r$  and  $t$  are both smaller than  $L_D$ , the hopfion cannot be stabilized in the nanodisk and MAP

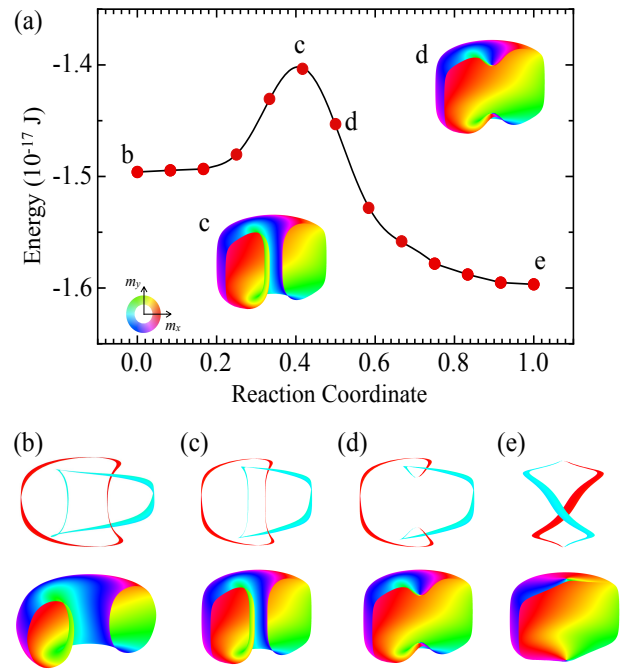


FIG. 5. (a) Minimal energy path between the hopfion and MAP state. Points b and e represent the hopfion and the MAP, respectively. The hopfion is nearly annihilated at saddle point c, and the MAP is created at d. Insets show the half-plane view preimages of  $s_z = 0$  for spin textures at c and d. (b)-(e) Top panel: The preimages of  $\mathbf{s} = (-1, 0, 0)$  (cyan) and  $\mathbf{s} = (1, 0, 0)$  (red) corresponding to points b–e in (a). Bottom panel: The half-plane view preimages of  $s_z = 0$  corresponding to points b–e in (a). The nanodisk geometry is the same as in Fig. 1.

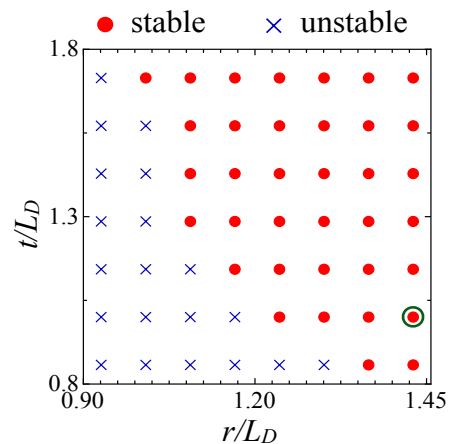


FIG. 6. Phase diagram of hopfion in chiral magnet nanodisk with various radius  $r$  and thickness  $t$ . The circled dot indicates the geometry used in Figs. 1, 3, and 5.

is the ground state. As  $r$  and  $t$  increase, the MAP state continues to be the ground state, but the hopfion appears as a metastable state and it remains the metastable state with increasing  $r$  and  $t$  for the values shown in Fig. 6. As  $r$  and  $t$  continue to increase, multiple MAP states, multiple hopfion states and more complicated spin textures appear. These results illustrate the effect of 3D confinement on the hopfion stability, and they provide a set of geometry parameters for experimentally achieving a stable hopfion in chiral magnet nanodisks.

## VI. CONCLUSIONS

To conclude, in a chiral magnet nanodisk sandwiched by two magnetic layers with PMA, two stable states exist at zero external magnetic field, a MAP state and a  $Q_H = 1$  hopfion state. The ratio of the helical period  $L_D$  to the disk radius and thickness determines the stability of hopfion. Although the MAP state is the ground state of the nanodisk, it can be switched into the metastable hopfion state by applying a magnetic field. The minimal energy path calculation reveals the topological transition and the energy barrier between the hopfion and the MAP state. 3D magnetic imaging techniques such as the X-ray vector nanotomography could be a powerful tool for visualizing the spin texture of hopfion in real space [43]. The hopfion may exhibit fascinating electronic transport and dynamical properties due to its novel topology. This work paves a way in the development of 3D spintronics and high dimensional memory architectures [44].

## ACKNOWLEDGEMENTS

JZ acknowledges stimulating discussions with Jeffrey Teo. The authors thank Paul Suttcliffe for fruitful discussions. Conception and analytical works in this work were supported by the U.S. Department of Energy (DOE), Office of Science, Basic Energy Sciences (BES) under Award No. DE-SC0016424. Numerical simulations and part of the analytical work were supported as part of the Spins and Heat in Nanoscale Electronic Systems (SHINES) an Energy Frontier Research Center funded by the U.S. Department of Energy, Office of Science, Basic Energy Sciences under Award No. DE-SC0012670. Collaborative travel between UCR and UNH were also supported by the NSF ECCS-1408168.

## APPENDIX A: DETAILS OF THE SIMULATIONS

The micromagnetic simulations were carried out using Mumax3 [45], and the results were also verified in terms of atomistic spin simulation carried out by Fidimag [46] and an in-house micromagnetic simulation package. For the chiral magnet nanodisk, we take

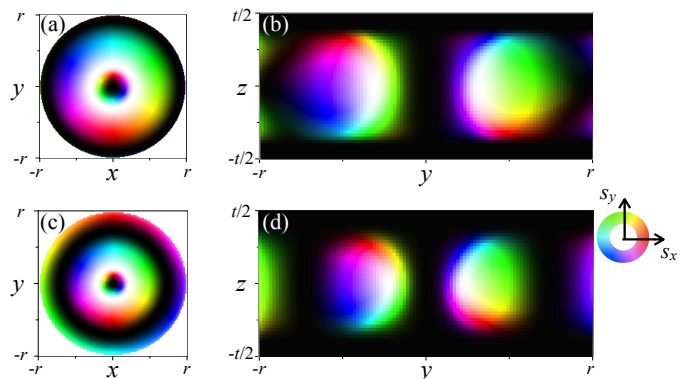


FIG. 7. (a), (c) The cross-sectional spin textures in the  $x$ - $y$  plane ( $z=0$ ) for hopfion with (a) and without (c) DDI. (b), (d) The cross-sectional spin textures in the  $y$ - $z$  plane ( $x=0$ ) for hopfion with (b) and without (d) DDI. Here the nanodisk has radius  $r = 1.43L_D$  and thickness  $t = 1L_D$ .

the exchange constant  $A = 2.195$  pJ/m, DMI constant  $D = 0.395$  mJ/m<sup>2</sup> and saturation magnetization  $M_s = 384$  kA/m. A perpendicular magnetic anisotropy constant  $K_u = 0.8$  MJ/m<sup>3</sup> is used for the magnetic thin nanodisks at the top and bottom. In micromagnetic simulations, the mesh cell size was varied from  $2 \text{ nm} \times 2 \text{ nm} \times 2 \text{ nm}$  to  $0.5 \text{ nm} \times 0.5 \text{ nm} \times 0.5 \text{ nm}$ , but the final results do not depend on the cell size.

Atomistic spin simulation was also employed to further verify the stability of the monopole-antimonopole (MAP) state. A lattice constant equal to 0.6 nm, the smallest size limited by our computer memory, was employed in the atomistic spin simulation and the magnetic interactions were adjusted from the micromagnetic parameters in order to fit this lattice constant. The dipole-dipole interaction (DDI) was also taken into account in the atomistic spin simulations. The atomistic spin simulations give similar results of MAP and hopfion and further confirm their stabilities.

Multiple initial states were employed in the simulations: a ferromagnetic state, a random state, a skyrmion tube at the center of the nanodisk, and a skyrmion tube in the chiral magnet part sandwiched by spin polarized states at the top and bottom magnetic layers with the spin polarization either parallel or antiparallel. Both the conjugate gradient method and the micromagnetic method are employed for the energy minimization. For the field induced switching part, hopfion and MAP initial states with different polarizations are used. After minimizing the energy at each field, we compare the energy of different states in order to get the switching diagram in the main text.

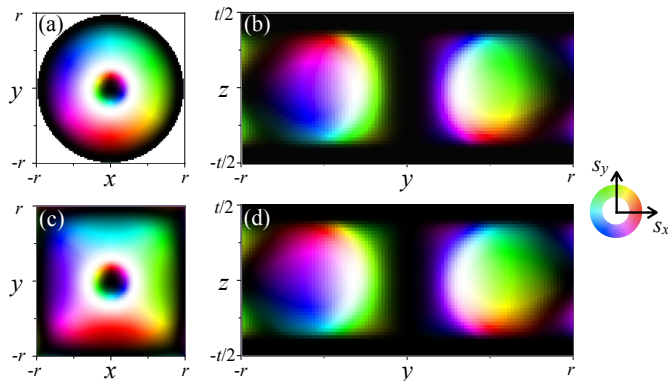


FIG. 8. (a), (c) The cross-sectional spin textures in the  $x$ - $y$  plane ( $z=0$ ) for hopfion in a circular disk (a) and in a square domain (c). (b), (d) The cross-sectional spin textures in the  $y$ - $z$  plane ( $x=0$ ) for hopfion in a circular disk (b) and in a square domain (d). Here the nanodisk has radius  $r = 1.43L_D$  and thickness  $t = 1L_D$  and the square domain has length  $l = 1.43L_D$  and thickness  $t = 1L_D$ .

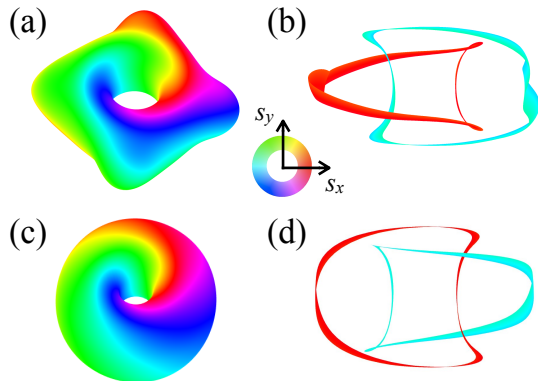


FIG. 9. (a), (c) The set of preimages with  $s_z = 0$  for hopfion in a circular disk (a) and in a square domain (c). The preimages of  $\mathbf{s} = (-1, 0, 0)$  (cyan) and  $\mathbf{s} = (1, 0, 0)$  (red) for the hopfion in a circular disk (b) and in a square domain (d).

## APPENDIX B: EFFECT OF THE DIOPLE-DIOPLE INTERACTION

In confined geometries, the DDI depends on the exact shape of the given geometry. The role of DDI in determining the explicit spin texture and Hopf charge of the hopfion is discussed in this section. We first check the DDI effect in a chiral magnet nanodisk with radius  $r = 100$  nm ( $1.43L_D$ ) and thickness  $t = 70$  nm ( $1L_D$ ), where  $L_D$  is the helical period in the chiral magnet. The hopfion spin textures with and without DDI are shown in Fig. 7. In the absence of DDI, although the hopfion is still stable, its configuration slightly differs. The hopfion is smaller than that in the presence of DDI. Furthermore, the edge states at the disk boundary are different in these two cases. In the presence of DDI, the edge de-

viates from  $z$ -direction only at two green (purple) islands shown in the left (right) edge in Fig. 7(b). In contrast, edge spins deviates from  $z$ -direction in a significant portion of boundaries in the absence of DDI, as shown in Fig. 7(d). Due to this reason, the cross-sectional spin texture in the  $x$ - $y$  plane at  $z=0$  only shows one concentric helical ring wrapping a skyrmion at the center in the presence of DDI, while two concentric rings are identified in the absence of DDI. The Hopf charge is 0.97 and 0.96 in the absence and presence of DDI respectively. Therefore, the DDI can indeed affects the morphology of hopfion, but has a minor effect on the Hopf charge.

Also we have checked the DDI effect with a square domain, which is different from the circular nanodisk discussed in the main text. As shown in Fig. 8, due to the DDI effect (or in other words, the shape anisotropy), the shape of the hopfion clearly reflects the shape of the square domain. The cross-sectional spin textures in the  $x$ - $y$  plane at  $z=0$  for both the circular disk and the square domain have the same topology, including a skyrmion at the disk center and a concentric helical ring. However, the helical ring in the square domain demonstrates an obvious square shape. Other than the spin textures, we further checked preimages of this new hopfion. The set of preimages of all spins with  $s_z = 0$  are plotted in Fig. 9(a) and (c). The shape of these preimages further confirms the effect of DDI. Although their shapes are different, the topology of hopfion, qualitatively described in terms of the genus and linking number, is still the same in circular disk and the square domain. The Hopf charge in the square domain is 0.92, which is smaller than the 0.96 in circular disk. Such slight difference comes from more complex edge states in the square domain.

## APPENDIX C: NUMERICAL CALCULATION OF HOPF INVARIANT

In real space, the integral form of Hopf invariant is defined as [38]

$$H = - \int \mathbf{B}(\mathbf{r}) \cdot \mathbf{A}(\mathbf{r}) d\mathbf{r}, \quad (3)$$

with  $B_i = \frac{1}{8\pi} \epsilon_{ijk} \mathbf{n} \cdot (\nabla_j \mathbf{n} \times \nabla_k \mathbf{n})$ , and  $\nabla \times \mathbf{A} = \mathbf{B}$ , where  $\mathbf{B}$  is the emergent magnetic field in form of the Levi-Civita symbol and  $\mathbf{A}$  is the gauge potential that satisfied the magnetostatic equation.

To avoid solving for the explicit form of  $\mathbf{A}$ , we represent  $\mathbf{A}$  in form of  $\mathbf{B}$  in momentum space. To do this, we first perform Fourier transformation on both  $\mathbf{A}$  and  $\mathbf{B}$  and get

$$\begin{aligned} \mathbf{A}(\mathbf{r}) &= \frac{1}{N} \sum \mathbf{A}(\mathbf{k}) e^{i2\pi\mathbf{k}\cdot\mathbf{r}}, \\ \mathbf{B}(\mathbf{r}) &= \frac{1}{N} \sum \mathbf{B}(\mathbf{k}) e^{i2\pi\mathbf{k}\cdot\mathbf{r}}, \end{aligned} \quad (4)$$

where  $N$  is the grid size of the system. The magnetostatic

equation in momentum space becomes

$$i2\pi\mathbf{k} \times \mathbf{A}(\mathbf{k}) = \mathbf{B}(\mathbf{k}). \quad (5)$$

Then, by using the Lagrange formula and the gauge re-

lation  $\mathbf{k} \cdot \mathbf{A} = 0$ , we solve Eq. 5 and get the expression

$$\mathbf{A}(\mathbf{k}) = -i \frac{\mathbf{k} \times \mathbf{B}(\mathbf{k})}{2\pi\mathbf{k}^2}. \quad (6)$$

Substituting Eq. 6 into Eq.(1), the Hopf invariant in momentum space becomes

$$H = i \frac{1}{N} \sum_{\mathbf{k}} \frac{\mathbf{B}(-\mathbf{k}) \cdot (\mathbf{k} \times \mathbf{B}(\mathbf{k}))}{2\pi\mathbf{k}^2}. \quad (7)$$

All the Hopf invariant calculations in the main text were obtained using Eq. 7.

- 
- [1] N. Manton and P. Sutcliffe, *Topological Solitons* (Cambridge University Press, Cambridge, England, 2004).
- [2] T. H. R. Skyrme, Nucl. Phys. **31**, 556 (1962).
- [3] R. Rajaraman, *Solitons and Instantons* (North-holland, Amsterdam, Netherlands, 1987).
- [4] G. Volovik and V. Mineev, Sov. Phys. JETP **46**, 401 (1977).
- [5] R. A. Battye and P. M. Sutcliffe, Phys. Rev. Lett. **81**, 4798 (1998).
- [6] R. A. Battye and P. M. Sutcliffe, Proc. R. Soc. A **455**, 4305 (1999).
- [7] H. Hopf, Math. Ann. **104**, 637 (1931).
- [8] P. Hilton, *An Introduction to Homotopy Theory* (Cambridge University Press, Cambridge, England, 1953).
- [9] L. Faddeev and A. J. Niemi, Nature **387**, 58 (1997).
- [10] L. Faddeev and A. J. Niemi, arXiv:hep-th/9705176 (1997), arXiv: hep-th/9705176.
- [11] D. Kleckner and W. T. M. Irvine, Nat. Phys. **9**, 253 (2013).
- [12] D. Kleckner, L. H. Kauffman, and W. T. M. Irvine, Nat. Phys. **12**, 650 (2016).
- [13] M. R. Dennis, R. P. King, B. Jack, K. O'Holleran, and M. J. Padgett, Nat. Phys. **6**, 118 (2010).
- [14] Y. Kawaguchi, M. Nitta, and M. Ueda, Phys. Rev. Lett. **100**, 180403 (2008).
- [15] P. J. Ackerman, J. van de Lagemaat, and I. I. Smalyukh, Nat. Commun. **6**, 6012 (2015).
- [16] P. J. Ackerman and I. I. Smalyukh, Nat. Mater. **16**, 426 (2017).
- [17] D. S. Hall, M. W. Ray, K. Tiurev, E. Ruokokoski, A. H. Gheorghie, and M. Möttönen, Nat. Phys. **12**, 478 (2016).
- [18] I. Dzyaloshinsky, J. Phys. Chem. Solids **4**, 241 (1958).
- [19] T. Moriya, Phys. Rev. **120**, 91 (1960).
- [20] U. K. Röfler, A. N. Bogdanov, and C. Pfeleiderer, Nature **442**, 797 (2006).
- [21] A. Fert, V. Cros, and J. Sampaio, Nat. Nanotech. **8**, 152 (2013).
- [22] F. Jonietz, S. Mhlbauer, C. Pfeleiderer, A. Neubauer, W. Mnzer, A. Bauer, T. Adams, R. Georgii, P. Bni, R. A. Duine, K. Everschor, M. Garst, and A. Rosch, Science **330**, 1648 (2010).
- [23] N. R. Cooper, Phys. Rev. Lett. **82**, 1554 (1999).
- [24] P. Sutcliffe, Phys. Rev. B **76**, 184439 (2007).
- [25] A. B. Borisov and F. N. Rybakov, JETP Lett. **88**, 264 (2008).
- [26] J.-S. B. Tai, P. J. Ackerman, and I. I. Smalyukh, PNAS , 201716887 (2018).
- [27] P. Sutcliffe, Phys. Rev. Lett. **118**, 247203 (2017).
- [28] I. I. Smalyukh, Y. Lansac, N. A. Clark, and R. P. Trivedi, Nature Materials **9**, 139 (2010).
- [29] H. Du, W. Ning, M. Tian, and Y. Zhang, Europhys. Lett. **101**, 37001 (2013).
- [30] A. O. Leonov, U. K. Röfler, and M. Mostovoy, EPJ Web Conf. **75**, 05002 (2014).
- [31] M. Beg, R. Carey, W. Wang, D. Corts-Ortuo, M. Vousden, M.-A. Bisotti, M. Albert, D. Chernyshenko, O. Hovoroka, R. L. Stamps, and H. Fangohr, Sci. Rep. **5**, 17137 (2015).
- [32] F. Zheng, H. Li, S. Wang, D. Song, C. Jin, W. Wei, A. Kovcs, J. Zang, M. Tian, Y. Zhang, H. Du, and R. E. Dunin-Borkowski, Phys. Rev. Lett. **119**, 197205 (2017).
- [33] See Supplemental Materials, for details of the simulations, effect of DDI, Hopf invariant calculations and movies for the topological transition. Micromagnetic and atomistic spin simulations were performed using Mumax3 [45], Fidimag [46] and an in-house simulation package.
- [34] A. Bogdanov and A. Hubert, J. Magn. Magn. Mater. **195**, 182 (1999).
- [35] Spirit spin simulation framework, (see <https://spirit-code.github.io>).
- [36] J. W. Milnor, *Topology from the Differentiable Viewpoint* (Princeton University Press, Princeton, 1997).
- [37] J. H. C. Whitehead, Proc. Natl. Acad. Sci. U.S.A. **33**, 117 (1947).
- [38] F. Wilczek and A. Zee, Phys. Rev. Lett. **51**, 2250 (1983).
- [39] J. E. Moore, Y. Ran, and X.-G. Wen, Phys. Rev. Lett. **101**, 186805 (2008).
- [40] P. F. Bessarab, V. M. Uzdin, and H. Jónsson, Comput. Phys. Commun. **196**, 335 (2015).
- [41] D. Cortés-Ortuño, W. Wang, M. Beg, R. A. Pepper, M.-A. Bisotti, R. Carey, M. Vousden, T. Kluyver, O. Hovoroka, and H. Fangohr, Sci. Rep. **7**, 4060 (2017).
- [42] P. F. Bessarab, G. P. Müller, I. S. Lobanov, F. N. Rybakov, N. S. Kiselev, H. Jónsson, V. M. Uzdin, S. Blügel, L. Bergqvist, and A. Delin, arXiv:1706.07173 [cond-mat] (2017), arXiv: 1706.07173.
- [43] C. Donnelly, M. Guizar-Sicairos, V. Scagnoli, S. Gliga, M. Holler, J. Raabe, and L. J. Heyderman, Nature **547**, 328 (2017).
- [44] A. Fernández-Pacheco, R. Streubel, O. Fruchart, R. Hertel, P. Fischer, and R. P. Cowburn, Nat. Commun. **8**,

- 15756 (2017).
- [45] A. Vansteenkiste, J. Leliaert, M. Dvornik, M. Helsen, F. Garcia-Sanchez, and B. Van Waeyenberge, *AIP Advances* **4**, 107133 (2014).
- [46] D. Cortés-Ortuño, W. Wang, R. Pepper, M.-A. Bisotti, T. Klyuyver, M. Vousden, and H. Fangohr, *Fidimag v2.0*, Tech. Rep. (Zenodo, 2016) doi: 10.5281/zenodo.167858.